The multi-axial deformation behavior of bulk metallic glasses at high homologous temperatures

R. Ekambaram [a], P. Thamburaja [a,*], H. Yang [b], Y. Li [b], N. Nikabdullah [c]

[a] Department of Mechanical Engineering, National University of Singapore, Singapore 117576, Singapore
[b] Department of Materials Science, National University of Singapore, Singapore 117576, Singapore
[c] Department of Mechanical Engineering, Universiti Kebangsaan Malaysia, Bangi 43600, Malaysia

ABSTRACT

In this work, we study the behavior of a recently-developed Lanthanum-based bulk metallic glass under uniaxial and multi-axial stress-states using the constitutive model developed by Thamburaja and Ekambaram (2007). The material parameters in the constitutive model are fitted to match the stress–strain responses obtained from a set of simple compression experiments conducted at temperatures within the supercooled liquid region under a variety of strain rates spanning approximately three decades. With the material parameters calibrated, we show that the aforementioned constitutive model is able to accurately predict the force vs. displacement responses of representative experiments conducted under multi-axial stress-states at temperatures within the supercooled liquid region, namely three-point bending and the superplastic forming of a miniature gear component. In particular, the evolution of the specimen geometry during the deformation under multi-axial loading conditions are also well-predicted by the constitutive model.

© 2009 Elsevier Ltd. All rights reserved.

1. Introduction

Bulk metallic glasses (BMG) are finding increased used as components in the sporting goods, bio-medical equipment, electronics, transformers and MEMS industries (Wang et al., 2004). This is due to their ability in having more desirable properties compared to conventional metallic alloys e.g. no crystallographic defects, higher strength, higher wear resistance, softer magnetism, higher corrosion resistance, etc. (Roth et al., 2005). Although BMG specimens can be directly cast into the components' required final shape, certain commercial applications requires these as-cast BMGs to undergo a certain degree of metal forming process depending on the required final shape.

Typically, the forming of metallic glass components occur at temperatures within the *supercooled liquid region*, i.e. the temperature range between the *glass transition temperature* and the *crystallization temperature*. Compared to its behavior at temperatures well-below its glass transition temperature, BMGs have very low viscosities and exhibit fluid-like flow behavior at temperatures within the supercooled liquid region. Hence the superplastic forming of BMG components can easily be performed within this temperature range.

There have been extensive experimental investigations regarding the forming processes of BMGs into useful components. Kawamura et al. (1999) and Saotome et al. (2001) have studied the superplastic deformation of an La-based metallic glass in the supercooled liquid region. The micro-forming ability of Zr-based BMGs have also been investigated by Kawamura and Inoue (1999), Kim et al. (2004), Wang et al. (2005) and Lewandowski et al. (2006, 2008). Recently, Schroers (2008) has also studied the formability of a variety of BMGs within their respective supercooled liquid region. From these works it has been demonstrated that within the supercooled liquid region, BMGs exhibit excellent workability.

Metallic glass specimens typically undergo extensive deformations and experience multi-axial stress-states during superplastic forming into useful components. Therefore, the design process of these components can be optimized with the aid of computer simulations using a set of constitutive equations which are three-dimensional and finite-deformation-based in nature. Some of the earlier developed constitutive models for metallic glasses are the equations postulated by Spaepen (1977), Argon (1979), De Hey et al. (1997), Chen et al. (2000), and Kato et al. (2001). However, these constitutive models are one-dimensional in nature. The yielding in a Pd-based BMG has also been studied by Donovan (1989). Huang et al. (2002) have developed a three-dimensional and small-strain-based constitutive model for metallic glasses. A fictive-stress-based theory was used by Kim et al. (2004) to model the micro-forming process of a BMG within the supercooled liquid region.[1]

---

* Corresponding author. Tel.: +65 6874 5539; fax: +65 6779 6559.
  E-mail address: mpept@nus.edu.sg (P. Thamburaja).

[1] Actual details regarding the multi-dimensional fictive-stress constitutive model has not been provided in the paper of Kim et al. (2004).

Recently, Thamburaja and Ekambaram (2007) have developed a finite-deformation-based and thermo-mechanically-coupled constitutive model for metallic glasses. Their constitutive theory was derived using fundamental thermodynamic laws and the principle of micro-force balance (Fried and Gurtin, 1994). Furthermore, they have also implementer their constitutive model into the Abaqus (Abaqus, 2008) finite-element program. In this work, we shall use the constitutive model of Thamburaja and Ekambaram (2007) and its numerical-implementation into the Abaqus finite-element program to study the uniaxial and multi-axial deformation behavior of a recently-developed BMG system.

The plan of this paper is as follows: in Section 2, we summarize the key equations in the constitutive model of Thamburaja and Ekambaram (2007). In Section 3, we describe the procedure for the preparation of the raw BMG material, the experimental set-ups and provide details regarding the calibration of the constitutive parameters. In this Section, we will also present results obtained from a series of simple compression, three-point bending and superplastic forming experiments conducted on the BMG alloy. The results obtained from the numerical simulations of the aforementioned experiments will also be presented and discussed in Section 3. Finally, we conclude in Section 4.

2. Constitutive equations

Here we summarize the key constitutive equations from the constitutive model developed by Thamburaja and Ekambaram (2007). For more details regarding the development of the constitutive model, please refer to aforementioned work. All material parameters in the constitutive model are treated as constants unless stated otherwise.

The governing variables[2] in the constitutive model are: (i) The Helmholtz free energy per unit *reference* volume, ψ. (ii) Absolute temperature, θ. (iii) The deformation gradient, $\mathbf{F}$ with $\det \mathbf{F} > 0$. (iv) The plastic distortion, $\mathbf{F}^p$ with $\det \mathbf{F}^p > 0$. (v) The elastic distortion, $\mathbf{F}^e$ with $\mathbf{F}^e = \mathbf{F}\mathbf{F}^{p-1}$ and $\det \mathbf{F}^e > 0$. (vi) The elastic stretch, $\mathbf{U}^e$ with $\mathbf{U}^e = \mathbf{U}^{eT}$ and $\det \mathbf{U}^e > 0$. The spectral representation of the elastic stretch is given by $\mathbf{U}^e = \sum_{\alpha=1}^{3} \lambda_\alpha^e \, \mathbf{r}_\alpha \otimes \mathbf{r}_\alpha$ with $\{\lambda_\alpha^e | \alpha = 1, 2, 3\}$ representing the positive-valued *eigenvalues* and $\{\mathbf{r}_\alpha | \alpha = 1, 2, 3\}$ the mutually orthonormal *eigenvectors* of $\mathbf{U}^e$. (vii) The elastic rotation, $\mathbf{R}^e$ with $\mathbf{R}^e = \mathbf{R}^{e-T} = \mathbf{F}^e\mathbf{U}^{e-1}$ and $\det \mathbf{R}^e = 1$. (viii) The elastic logarithmic (Hencky) strain, $\mathbf{E}^e = (1/2) \ln \mathbf{C}^e$ where $\mathbf{C}^e = \mathbf{U}^{e2}$ represents the elastic right Cauchy-Green strain. (ix) The Cauchy stress, $\mathbf{T}$ with $\mathbf{T} = \mathbf{T}^T$. (x) The work-conjugate stress to the elastic strain $\mathbf{E}^e$, $\mathbf{T}^*$ with $\mathbf{T}^* = (\det \mathbf{F})\mathbf{R}^{eT} \mathbf{T} \mathbf{R}^e$ (xi) The plastic shear strain, $\gamma \geqslant 0$. (xii) The free volume concentration (units of volume per unit volume), $\xi \geqslant 0$.

2.1. Free energy

The Helmholtz free energy density, ψ is taken to be in the separable form

$$\psi = \hat{\psi}(\mathbf{C}^e, \theta, \nabla\xi, \xi) = \psi^e + \psi^\theta + \psi^g + \psi^\xi \quad \text{with} \tag{1}$$

$$\psi^e = \hat{\psi}^e(\mathbf{C}^e, \theta)$$
$$= \mu|\text{dev } \mathbf{E}^e|^2 + \kappa[(1/2) \text{ trace } \mathbf{E}^e - 3\alpha_{th}(\theta - \theta_o)] \text{ trace } \mathbf{E}^e, \tag{2}$$

$$\psi^\theta = \hat{\psi}^\theta(\theta) = c[(\theta - \theta_o) - \theta \, \ln (\theta/\theta_o)], \tag{3}$$

$$\psi^g = \hat{\psi}^g(\nabla\xi) = (1/2)s_{\xi1}|\nabla\xi|^2, \qquad \psi^\xi = \hat{\psi}^\xi(\xi, \theta)$$
$$= (1/2)s_{\xi2} \, \xi^2 - s_{\xi2} \, \xi \, \xi_T. \tag{4}$$

Here the variables $\psi^e, \psi^\theta, \psi^g$ and ψ^ξ represent the *thermo-elastic*, *purely thermal*, *gradient* and *flow-defect* free energies, respectively. The material constants $\mu > 0, \kappa > 0$ and α_{th} represent the shear modulus, bulk modulus and the linear thermal expansion coefficient, respectively. The specific heat per unit volume is denoted by $c > 0$. The material parameter $s_{\xi1} \geqslant 0$ (units of energy per unit length) represents the coefficient that amplifies the changes in the gradient free energy, ψ^g due to variations in $\nabla\xi$. The material parameter $s_{\xi2} \geqslant 0$ (units of energy per unit volume) represents the coefficient that amplifies the changes in the flow-defect free energy, ψ^ξ due to variations in ξ. Finally, ξ_T denotes the thermal equilibrium free volume concentration which can be approximated by a Vogel-Fulcher-Tammann (VFT)-like linear in temperature function (Masuhr et al., 1999):

$$\xi_T = \xi_g + k_\theta[\theta - \theta_g] \tag{5}$$

where θ_g is the *glass transition* temperature, ξ_g the thermal equilibrium free volume concentration at θ_g, and k_θ (units of temperature inverse) a constant of proportionality.

2.2. Stress–strain constitutive equation

The constitutive equation for the stress $\mathbf{T}^*$ is given by

$$\mathbf{T}^* = 2 \, \mathbf{U}^e \left(\frac{\partial\psi}{\partial\mathbf{C}^e}\right) \mathbf{U}^e$$
$$= 2\mu[\text{dev } \mathbf{E}^e] + \kappa[\text{trace } \mathbf{E}^e - 3\alpha_{th}(\theta - \theta_o)]\mathbf{1}. \tag{6}$$

2.3. Flow rule

The flow rule provides the evolution equation for the plastic distortion, $\mathbf{F}^p$. With the variable $\mathbf{L}^p$ denoting the *plastic velocity gradient*, we write the flow rule as:

$$\dot{\mathbf{F}}^p = \mathbf{L}^p\mathbf{F}^p \quad \text{where} \quad \mathbf{L}^p = \dot{\gamma}\sqrt{\frac{1}{2}}\left(\frac{\text{dev } \mathbf{T}^*}{|\text{dev } \mathbf{T}^*|}\right) + \dot{\xi}\left(\frac{1}{3}\right)\mathbf{1}. \tag{7}$$

The quantities $\dot{\gamma} \geqslant 0$ and $\dot{\xi}$ represent the plastic shear strain-rate and the free volume generation rate, respectively.

2.4. Evolution equation for the plastic shear strain

The expression for the plastic shear strain-rate is given by

$$\dot{\gamma} = 2f_o \, \exp\left\{-\frac{Z}{k_b\theta} - \frac{\varphi}{\xi}\right\} \sinh\left[\frac{\bar{\tau}\Omega}{2k_b\theta + (\chi\bar{p} + \zeta_f\bar{\tau}_v) \, \Omega}\right] \tag{8}$$

with $\bar{\tau} = \sqrt{1/2} \, \|\text{dev } \mathbf{T}^*| \geqslant 0$, $\bar{p} = -(1/3) \text{ trace } \mathbf{T}^*$ and $\bar{\tau}_v = s_{\xi2} (\xi - \xi_T) - s_{\xi1}(\nabla^2\xi)$ denoting the equivalent shear stress, the hydrostatic pressure and the viscous stress, respectively. The parameters f_o (units of time inverse) denote the frequency of atomic vibration, $Z > 0$ the activation energy (units of energy), k_b the Boltzmann constant, $\Omega > 0$ the activation volume (units of volume), $\varphi > 0$ a unitless geometric overlap factor, and χ the pressure-sensitivity parameter. The dimensionless fit parameter, ζ_f determines the sensitivity of the plastic flow to the viscous stress, $\bar{\tau}_v$.

2.5. Kinetic equation for the free volume concentration

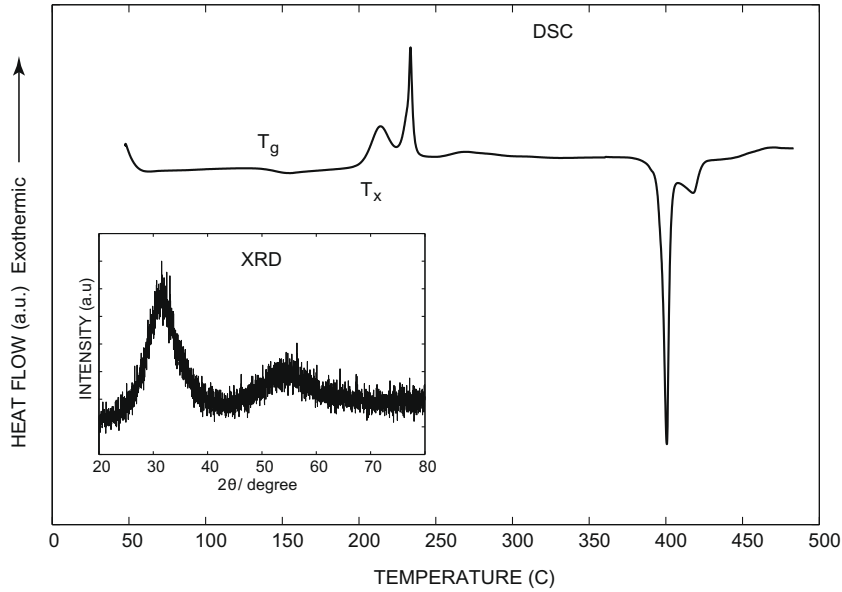The diffusion–creation–annihilation equation for the free volume concentration is

---

[2] *Notation*: ∇ and ∇^2 denote the *referential* gradient and the *referential* Laplacian, respectively. The inverse of a second-order tensor $\mathbf{B}$ is denoted by $\mathbf{B}^{-1}$. The transpose of tensor $\mathbf{B}$ is denoted by $\mathbf{B}^T$, and $(\mathbf{B}^{-1})^T = \mathbf{B}^{-T}$. The determinant of the tensor $\mathbf{B}$ is denoted by $\det \mathbf{B}$. The second-order identity tensor is denoted by $\mathbf{1}$. The trace of the tensor $\mathbf{B}$ is denoted by trace $\mathbf{B} = \mathbf{1} \cdot \mathbf{B}$. The magnitude of the tensor $\mathbf{B}$ is denoted by $|\mathbf{B}| = \sqrt{\mathbf{B} \cdot \mathbf{B}}$. The deviatoric (traceless) portion of tensor $\mathbf{B}$ is denoted by dev $\mathbf{B} = \mathbf{B} - (1/3)[\text{trace } \mathbf{B}]\mathbf{1}$.

Fig. 1. The DSC data for $La_{61.4}Al_{15.9}Ni_{11.35}Cu_{11.35}$ amorphous alloy, obtained using a scanning rate of 20 °K/min. The inset represents the XRD pattern for the same alloy, indicating the amorphous nature of the as-cast specimen.

$$\dot{\xi} = \left(\frac{\dot{\gamma}_o s_{\xi 1}}{s_{\xi 3}}\right)\left(\nabla^2 \xi\right) + \zeta\dot{\gamma} - \left(\frac{\dot{\gamma}_o \bar{p}}{s_{\xi 3}}\right) - \left(\frac{\dot{\gamma}_o s_{\xi 2}}{s_{\xi 3}}\right)(\xi - \xi_T) \qquad (9)$$

where $\dot{\gamma}_o = f_o \exp\{-\frac{Z}{k_b\theta} - \frac{\varphi}{\xi}\}$. With respect to the terms on the right-hand side of Eq. (9), the first term is the *diffusion* of free volume, the second term is the *creation* of free volume by plastic deformation, the third term is the generation of free volume due to *hydrostatic pressure*, and the fourth term is the generation of free volume by *structural relaxation*. Here $s_{\xi 3} > 0$ (units of energy per unit volume) represents the *resistance* to free volume generation due to free volume diffusion, hydrostatic pressure and structural relaxation. Finally, $\zeta = \hat{\zeta}(\bar{\tau}) \geqslant 0$ represents the dimensionless free volume creation parameter.

2.6. Balance of energy

From the first law of thermodynamics, we obtain:

$$\dot{\theta} = c^{-1}\left\{k_{th}\left(\nabla^2\theta\right) + \dot{r} - 3\kappa\alpha_{th}\left\{\text{trace } \dot{\mathbf{E}}^e\right\}\theta - s_{\xi 2}k_\theta\dot{\xi}\theta + \dot{\omega}\right\} \qquad (10)$$

where $\dot{\omega} = \bar{\tau}\dot{\gamma} + [s_{\xi 1}(\nabla^2\xi) - s_{\xi 2}(\xi - \xi_T) - \bar{p}]\dot{\xi} \geqslant 0$ represents the rate of plastic dissipation per unit *reference* volume, $\dot{r}$ the *referential* heat supply rate per unit volume, and $k_{th} = \hat{k}_{th}(\theta) > 0$ the thermal conductivity coefficient. In Eq. (10), the Taylor-Quinney coefficient, i.e. the fraction of plastic work rate converted into heating is unity.

To summarize, the list of constitutive parameters/functions needed to be calibrated are

$$\{\mu, \kappa, \alpha_{th}, s_{\xi 1}, s_{\xi 2}, s_{\xi 3}, \chi, \zeta, \xi_g, k_\theta, \theta_g, \zeta_f, f_o, \varphi, Z, \Omega, c, k_{th}, \dot{r}\}.$$

A time-integration procedure based on the constitutive model for metallic glasses listed above has been developed and implemented in the Abaqus (2008) finite-element program by writing a user-material subroutine.

3. Experimental procedure and finite-element simulations

The focus of the present work is on the modeling of the $La_{61.4}Al_{15.9}Ni_{11.35}Cu_{11.35}$ BMG system developed by Tan et al. (2003). We choose this alloy for our present study due to its combined advantages of having a relatively lower glass transition temperature ($\theta_g \approx 410$ K) compared to other families of metallic glasses, its wider super cooled liquid region (approximately 70 K) and its high glass-forming ability with a critical thickness of 10.5 mm. The raw materials La (99.9%), Al(99.9%), Ni(99.98%) and Cu(99.9999%) were used for preparing metallic glass plates having dimensions of 80 mm× 30 mm × 5 mm. The alloy mixture placed in a quartz crucible is melted by means of an induction furnace. The molten alloy is subsequently chill cast by pouring it into a copper mold in presence of a high purity argon atmosphere. The cast specimens are subsequently examined using X-ray diffraction (XRD) in order to verify the glassy nature of the as-cast sample. Furthermore, the critical temperatures for this alloy are determined by carrying out a Differential Scanning Calorimetry (DSC) study of the as-cast specimen. The DSC test was done by employing a continuous heating rate of 20 °K/min. The obtained results from the DSC analysis is shown in Fig. 1 with the inset figure depicting the corresponding XRD trace for the $La_{61.4}Al_{15.9}Ni_{11.35}Cu_{11.35}$ (La-based) metallic glass alloy. The DSC results identified the glass transition temperature, θ_g and the crystallization temperature, θ_x as 407 K and 479 K, respectively. The absence of any discrete crystalline peaks in the XRD result confirms that the alloy is fully amorphous. A note regarding XRD measurements: XRD technique is only capable of detecting crystalline structure when the volume fraction of crystallinity exceeds a few percent. The information on the amount of crystallinity is important since the flow property and pressure sensitivity of the metallic glass strongly depends on it.

The batch of test specimens required for the experiments were cut from the *same* as-cast metallic glass plate. In this work, we have performed three types of experiments on the La-based BMG in the supercooled liquid region: (a) simple compression, (b) three-point bending and (c) superplastic forming. The cuboidal specimens used for the simple compression experiments have initial dimensions of 4 mm × 4 mm × 8 mm. The three-point bending experiments were conducted on cuboidal specimens having initial dimensions of 4 mm × 6 mm × 45 mm. Finally, the superplastic forming experiments were performed on cylindrical specimens having initial dimensions of 5 mm in height and 4 mm diameter.

The surface of the specimens which comes into contact with the testing machines/die during testing are polished using 1200 grit silicon carbide paper, and a thin film of molybdenum disulphide

is coated on these surfaces to attain nearly-frictionless conditions during the high temperature experiments. All our experiments were carried out using an Instron 8874 type axial/torsional servo hydraulic system. The compression experiments were performed under true-strain-rate control conditions by using a 2620-604 type axial extensometer.

All the experiments in this work were conducted within the Instron 3119 series environmental chamber which has a working temperature range of up to 523 °K. The ambient environment around the specimen is still air. The required BMG specimen temperature for all the experiments were achieved by using a constant heating rate of 20 °K/min. An additional K-type thermocouple having an accuracy of 0.1 °K is placed next[3] to the metallic glass specimen to confirm the actual specimen temperature. Once the temperature of the specimen reaches the ambient test temperature, it is held at this temperature for exactly 10 min before the experiments are performed. We assume that this annealing procedure allows the free volume within the material to attain its thermal equilibrium value at the given ambient test temperature, i.e. $\xi_{t=0} \approx \xi_T$ (Lu et al., 2003).

In order to study the high temperature flow behavior of the La-based metallic glass and predict the experimental data using our constitutive model, we shall perform compression experiments at temperatures within the supercooled liquid region, ranging from 417 K to 432 K and at various strainrates ranging from 1×10^{-4}/s to 7×10^{-2}/s. Note that if the experimental applied strainrates are high enough, shear localization and fracture will still occur in the specimens. In this work, we will concentrate on modeling the deformation behavior of La-based metallic glasses in the absence of shear localization occurring in the test specimens. Using the constitutive theory presented in Section 2, we have also numerically-simulated the shear localization processes in bulk metallic glasses when deformed at high homologous temperatures (cf. Thamburaja and co-workers (2007, 2008, 2009)).

The set of constitutive parameters/functions for the La-based BMG alloy are determined by a combination of experimental data determined from literature and by fitting the constitutive model to a set of stress–strain data obtained from simple compression experiments conducted under various strain rates at different temperatures within the supercooled liquid region. It is important to note that the measurement of the experimental stress–strain curves were obtained by taking into account the compliance of the testing machine. The value for the machine compliance was obtained by compressing a block of hardened tool steel at the test temperatures of interest.

The density of the alloy calculated by Archimedes' principle is determined to be 6114 kg/m³. The value for Young's modulus is obtained by fitting our model to the average initial elastic slope of the stress strain experimental data at 417 K, it is determined to be 25 GPa. The approximate value for the Poisson's ratio of La-based metallic glasses is given in the work of Jiang et al. (2007) as 0.356. Hence the values for the shear modulus, μ and the bulk modulus, κ are 9.22 GPa and 28.93 GPa, respectively. For an La-based metallic glass (Kato et al., 2008) have identified the linear thermal expansion coefficient, α_{th} to be 15.3×10^{-6}/K.

For simplicity we assume the thermal conductivity coefficient and the specific heat capacity to be constants, and ignore their variations with respect to temperature. The specific heat capacity, c for an La-based metallic glass in the supercooled liquid region is determined from Jiang et al. (2007) as approximately 2.4 MJ/m³. The thermal conductivity coefficient is fit to the experimental stress–strain curves by performing coupled thermo-mechanical finite-element simulations (more on this later).

As an initial guess we shall use the value of 1.1×10^{24}/s for the frequency of atomic vibration, f_o (Ekambaram et al., 2008). The values of activation volume (Ω), activation energy (Z), geometric overlap factor (φ) and the constant of proportionality (k_θ) shall be determined following the same procedure outlined in Thamburaja and Ekambaram (2007), i.e. by conducting experiments at different temperatures under very low strain rates and low stresses in the Newtonian viscous limit. Under these conditions, the tensile viscosity, σ can be approximated by

$$\sigma \equiv \frac{3\bar{\tau}}{\dot{\bar{\gamma}}} \approx \left(\frac{3k_b \, \theta}{f_o \, \Omega}\right) \exp\left[\frac{Z}{k_b \, \theta} + \frac{\varphi}{\xi_T}\right] \quad \text{since}$$
$$2k_b\theta \gg (\chi\bar{p} + \zeta_f\bar{\tau}_v)\Omega. \tag{11}$$

The remaining unknowns in Eq. (11) are Ω, Z, φ and $\xi_T = \xi_g + k_\theta(\theta - \theta_g)$. Using typical values of $\Omega \sim 10^{-28}$m³, $Z \sim 10^{-19}$J, $\varphi \sim 0.1$, $\xi_T \sim 0.003$ and $k_\theta \sim 10^{-5}$K^{-1}, we heuristically fit Eq. (11) to the viscosity data obtained from the lowest (absolute-valued) strain-rate simple compression experiments conducted at temperatures 417 K, 422 K, 427 K and 432 K.[4] Once the range of the experimentally-determined viscosities are attained, the parameters are then fine-tuned to provide a better fit.

Based on the findings of Heggen et al. (2004), the free volume creation parameter, ζ is an increasing function of stress. As a first-cut approximation, assume an exponential form for the dependance of ζ on the stress and ignore its the temperature dependence:

$$\zeta = k_{\bar{\tau}} \exp\left(\frac{\bar{\tau}}{\bar{\tau}^*}\right). \tag{12}$$

Here, $k_{\bar{\tau}}$ and $\bar{\tau}^*$ (with units of stress) are the constants to be fit to match the strain softening region of the experimental stress–strain data.

Since the length scale for free volume diffusion is much smaller than the specimen sizes, we will neglect the effect of free volume diffusion in Eq. (9) by setting $s_{\xi 1} = 0.0$ MJ/m. For simplicity, the pressure-sensitivity parameter, χ is taken to be the same as the pressure-sensitivity of a Vitreloy-1 metallic glass, i.e. $\chi = 0.15$ (Patnaik et al., 2004).[5] Further using the methodology and modeling assumptions presented in Thamburaja and Ekambaram (2007), all the remaining material parameters $\{s_{\xi 2}, s_{\xi 3}, \zeta_f, \xi_*, k_{\bar{\tau}}, \bar{\tau}^*\}$ are then heuristically fitted to the experimental simple compression stress–strain data of specimens deformed under various (absolute-valued) strain rates ranging from 1×10^{-4}/s to 7×10^{-2}/s at different ambient temperatures within the supercooled liquid region as mentioned above.[6]

Assuming *homogeneous* deformations and *isothermal* conditions, a single Abaqus C3D8R continuum-three-dimensional brick element was used to conduct simple compression finite-element simulations to fit the material parameters listed in Table 1 to the aforementioned simple compression experimental stress–strain curves.[7] The initial conditions for *all* the finite-element simulations

---

[3] We were not able to permanently attach the thermocouple onto the specimens and therefore sliding between the thermocouple and the specimens may occur during the duration of the experiments.

[4] These viscosity data are assumed to be very close to the Newtonian viscosity data at temperatures of 417 K, 422 K, 427 K and 432 K.

[5] There are also various other works which deal with the effect of hydrostatic pressure/normal stress on the flow and fracture behavior of metallic glasses e.g. Davis and Kavesh (1975), Lewandowski and co-workers (1998, 1999, 2002), and Henann and Anand (2009). There are also experimental evidence which show increase in the pressure sensitivity with increasing temperature cf. Wesseling et al. (2008).

[6] The values for the material parameters $\{s_{\xi 2}, s_{\xi 3}, \zeta_f, \xi_*, k_{\bar{\tau}}, \bar{\tau}^*\}$ can be more accurately determined by fitting it to the stress–strain curves along with the free volume evolution data during plastic deformation. Since we were unable to experimentally measure the free volume evolution during deformation, we resort to fitting these parameters by heuristic means to achieve reasonable changes in free volume concentration during the deformation.

[7] The cross-section of the specimens were observed to be deforming homogenously during the simple compression experiments. Therefore the experimental stress–strain curves were calculated assuming homogeneous deformations.

Table 1
Material parameters for the La-based BMG

μ = 9.22 GPa	κ = 28.93 GPa	α_{th} = 15.3 × 10^{-6}/K
f_0 = 1.1 × 10^{24}/s	Z = 0.385 × 10^{-19} J	Ω = 2.52 × 10^{-28} m^3
φ = 0.325	χ = 0.15	ζ_f = 0.07
ξ_g = 5.58 × 10^{-3}	θ_g = 407 K	k_θ = 1.54 × 10^{-5}/K
$s_{\xi 2}$ = 3500 GJ/m^3	$s_{\xi 3}$ = 320 GJ/m^3	k_{th} = 5.0 W/mK
$\bar{\tau}_*$ = 115.5 MPa	$k_{\bar\tau}$ = 4.5 × 10^{-4}/Pa	c = 2.4 MJ/m^{3}K

are : (1) the free volume concentration at each material point has a value of the thermal equilibrium free volume concentration at the ambient test temperature, i.e. the material is initially-assumed to be fully-annealed, and (2) the plastic shear strain at each material point is zero. The fit of the constitutive model with respect to the experimental stress–strain curves are shown in Fig. 2. The overall experimental stress–strain curves are relatively-well-reproduced by the constitutive model. However, the stress–strain responses for the experiments conducted at the highest strain rates at test temperatures 422 K, 427 K and 432 K are not accurately reproduced by the constitutive model, i.e. the simulations are generally *over-predicting* the experimental steady-state stress levels.

To investigate this issue, we perform *coupled thermo-mechanical* finite-element simulations on the actual simple compression specimen geometry. Fig. 3a shows the initially-undeformed geometry of the simple compression specimen meshed using 686 Abaqus C3D8RT continuum-three-dimensional brick elements with temperature degree of freedom. The nodes on the bottom surface are constrained from motion along axis-3 whereas a velocity profile along axis-3 is imparted on the nodes at the top surface to simulate simple compression deformation at the desired strain-rate.

Initially, the temperature for *all* the nodes are set to the ambient test temperature of interest. The nodal temperatures on the top and bottom surfaces are maintained at the aforementioned ambient test temperature throughout the duration of the simulations. This is done as we have assumed the compression platens in contact with the specimen would act as an infinite heat sink. In all our coupled thermo-mechanical simulations, we have neglected (a) the heat supply rate term, $\dot{r}$, i.e. we set $\dot{r} = 0$, and (b) the heat convection from the specimens' side surfaces to the ambient environment (still air). Finally, all the coupled thermo-mechanical simulations in this work were conducted using the initially-undeformed finite-element mesh shown in Fig. 3a with each element initially having a free volume concentration being equal to the thermal equilibrium free volume concentration at the ambient test temperature of interest.

Using the material parameters listed in Table 1 along with a thermal conductivity coefficient of $k_{th} = 5.0$ W/mK, the predicted stress–strain responses from the coupled thermo-mechanical simple compression simulations are plotted in Figs. 3b–e along with the experimental stress–strain curves shown previously in Fig. 2. From Fig. 3, we can see that the experimental stress–strain curves obtained from the lower strain-rate experiments at all ambient test temperatures are almost identically well-predicted by both the coupled thermo-mechanical and isothermal finite-element simulations. However, the coupled thermo-mechanical simulations are predicting the higher strain-rate experiments' stress–strain curves for all ambient test temperatures more accurately compared to the isothermal simulations. The reason for this is as follows: Fig. 4 shows the temperature contours for the specimen once an applied compressive strain of 50% is attained. These contour plots were obtained from the simple compression coupled thermo-mechanical finite-element simulations that were conducted at ambient test
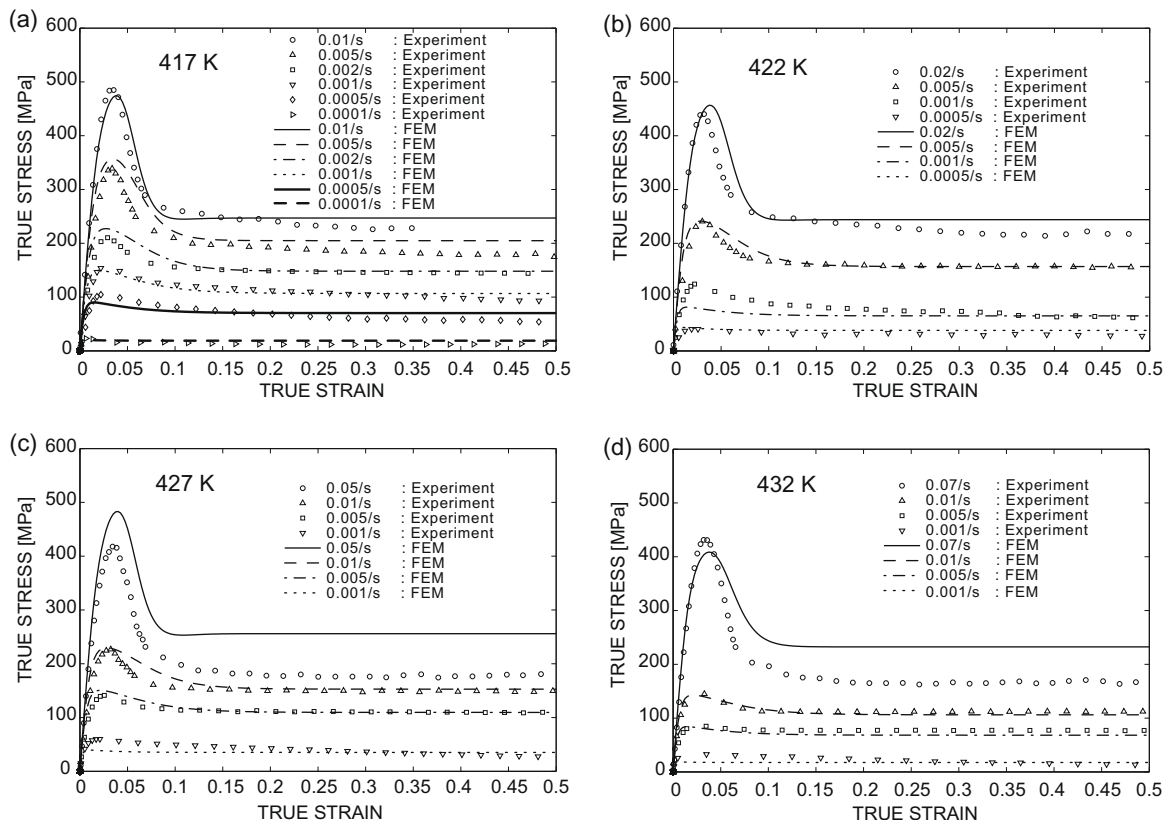

Fig. 2. Experimental stress–strain curves in simple compression at a temperatures of (a) 417 K, (b) 422 K, (c) 427 K, and (d) 432 K, under indicated strain rates. Also shown are the fitted stress–strain curves from the finite-element simulations conducted under isothermal conditions.
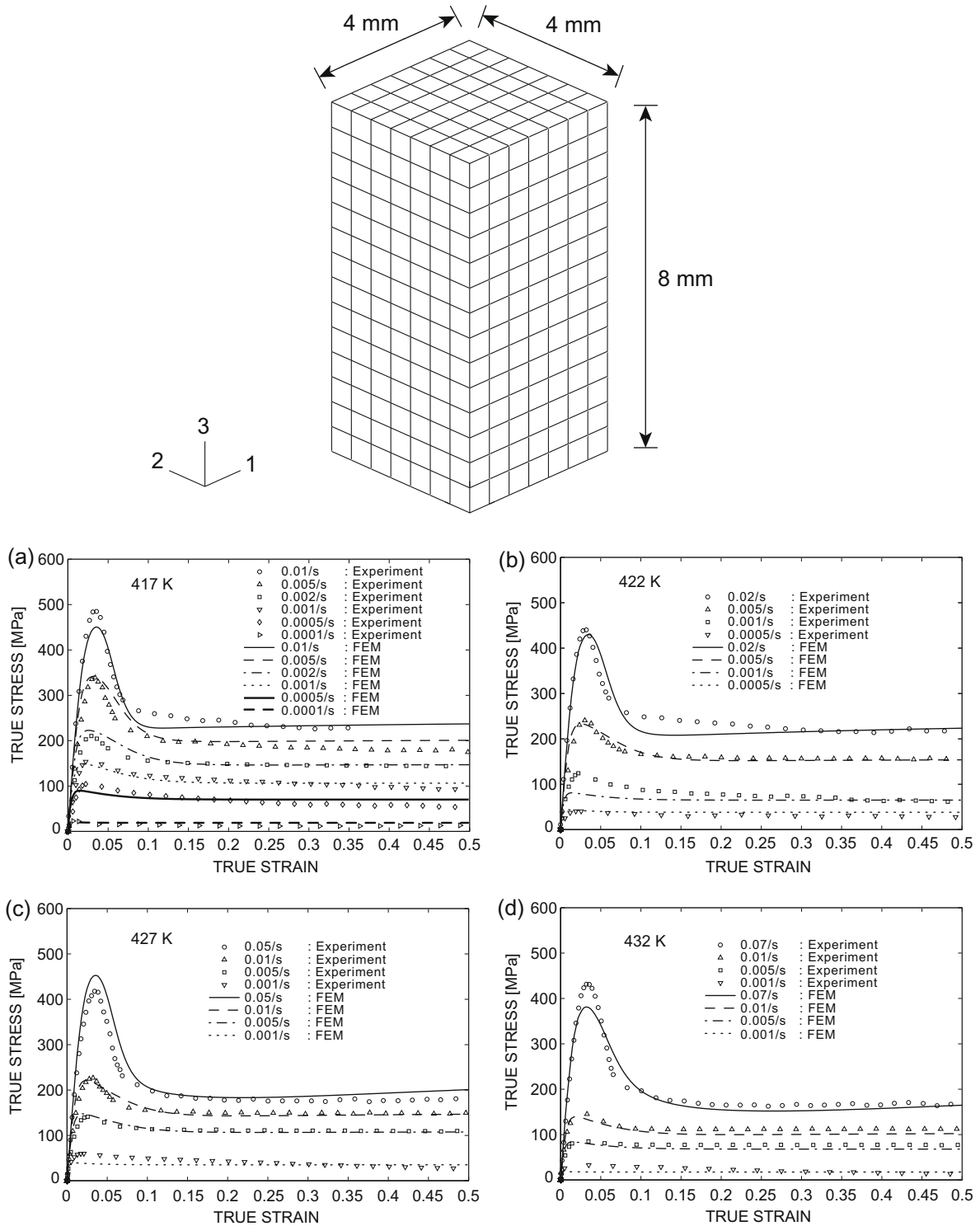
Fig. 3. Initial undeformed mesh of the compression test specimen having dimensions of 4 mm × 4 mm × 8 mm, using 686 Abaqus C3D8RT continuum-brick elements. (a) Experimental stress–strain curves in simple compression conducted at ambient test temperatures of (a) 417 K, (b) 422 K, (c) 427 K, and (d) 432 K under a variety of strain rates. Also shown are the predicted stress–strain curves from the coupled thermo-mechanical simulations.

temperatures of 417 K, 422 K, 427 K and 432 K under strain rates of 1×10^{-2}/s,2×10^{-2}/s,5×10^{-2}/s and 7×10^{-2}/s, respectively. From all the four temperature contour plots, we can generally see that the specimens have experienced a *rise* in temperature, measured with respect to the relevant ambient test temperature. This observed rise in the temperature is caused by the inability of the plastic dissipation, $\dot{\omega}$ to be conducted out of the specimen quickly enough. Since small changes in temperature can cause large changes in the plastic flow rate, i.e. Eq. (8), we can conclude that the overall reduction in the simulated stress levels are due to *thermal softening* effects. Hence thermal softening is the main cause for the differences in the calculated stress–strain curves shown in Fig. 2 vs. Fig. 3 especially for the simulations conducted at the highest strain rates at ambient test temperatures 422 K,
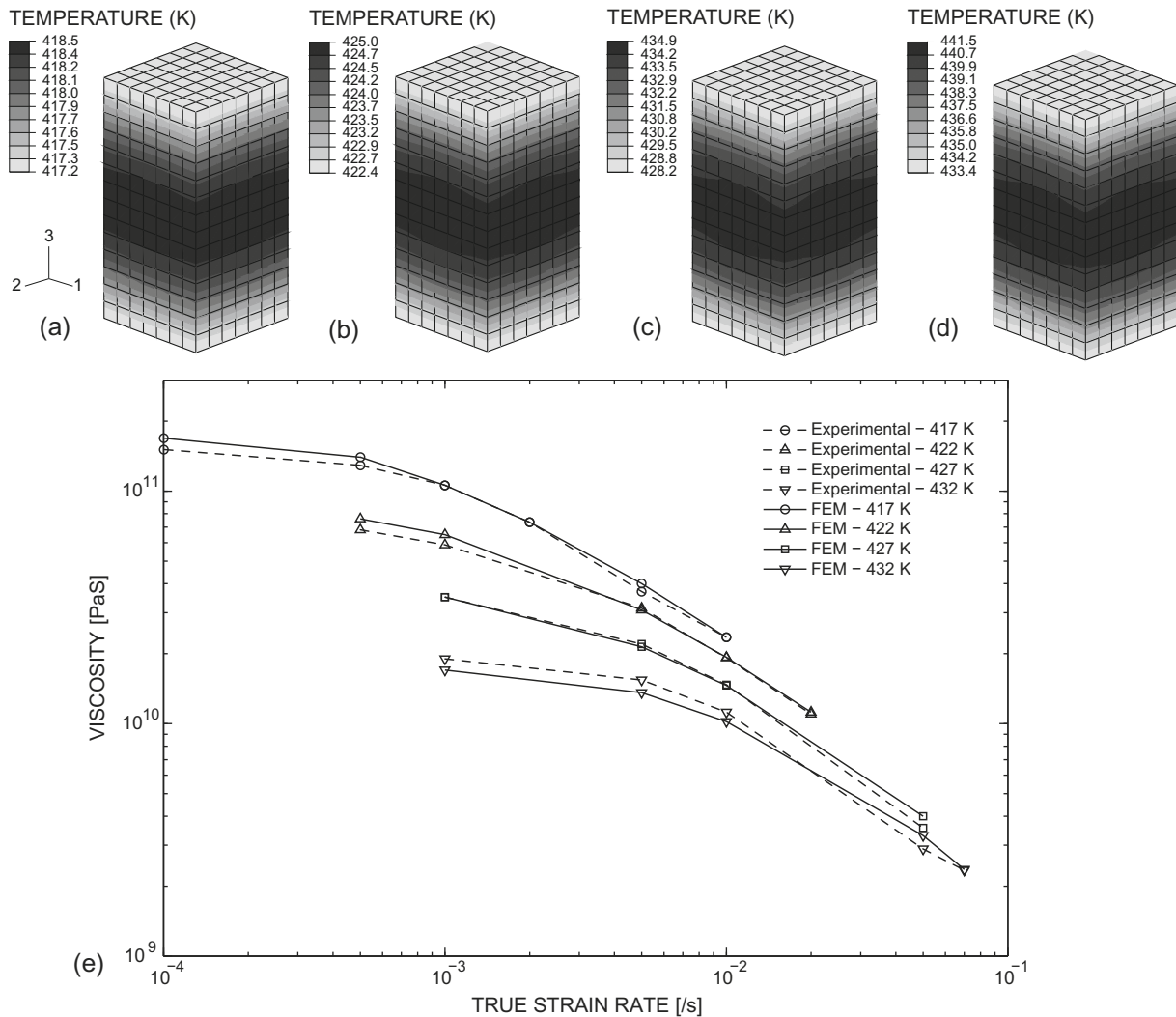
Fig. 4. Contours of the BMG specimen temperature at 50% compressive strain obtained from the finite-element simulations conducted at an (a) ambient temperature of 417 K and strain-rate of 1×10^{-2}/s, (b) ambient temperature of 422 K and strain-rate of 2×10^{-2} /s, (c) ambient temperature of 427 K and strain-rate of 5×10^{-2} /s, and (d) ambient temperature of 432 K and strain-rate of 7×10^{-2} /s. All the contour plots were drawn in the undeformed configuration for better visualization. (e) Experimentally obtained viscosity data for the La-based alloy over a range of strain rates and temperatures within the supercooled liquid region. Shown along with experimental data are the prediction using the coupled thermo-mechanical simulations.

427 K and 432 K. Also note that the differences in the simulated stress levels as shown in Fig. 2 vs. Fig. 3 at a given ambient test temperature and applied strain-rate is larger in the large applied strain range as compared to the small applied strain range. In the large applied strain range, a larger accumulation of plastic dissipation would have occurred. Therefore the coupled thermo-mechanical version of our theory would show a larger increase in the average specimen temperature in the large applied strain range as compared to small applied strain range *before* steady-state conditions are reached. As a result of this, thermal softening effects become more pronounced with increasing applied strain when the coupled thermo-mechanical version of the theory is used. Hence, when comparing the stress–strain response obtained from the isothermal vs. the coupled thermo-mechanical version of our constitutive theory, we will generally see increasing differences in the calculated stress levels with increasing applied strain.

From the experimental and simulated stress–strain curves shown in Fig. 3, we calculate the experimental steady-state tensile viscosity data and plot it with respect to the simulated steady-state viscosity data in Fig. 4e. From the results shown in Fig. 4e, we can see that the constitutive model is able to fit the experimentally-determined steady-state viscosity data to good accord. One final note

regarding the coupled thermo-mechanical simulations: the chosen value for the thermal conductivity coefficient of the Lanthanum-based BMG used in the present work at temperatures within the supercooled liquid region is reasonable since it is lower than the thermal conductivity coefficient of a Zr-based metallic glass within the same temperature range (≈ 8.0 W/mK from Demetriou and Johnson, 2004). This is due to Zirconium having a larger thermal conductivity coefficient compared to Lanthanum (Zhang et al., 2007).

3.1. Three point bending experiments and simulations

In this subsection, we aim to validate our constitutive model with respect to experiments conducted under multi-axial loading conditions at temperatures within the supercooled liquid region. To impart a multi-axial stress-state on the La-based metallic glass during its deformation, we have chosen to conduct three-point bending-type forming experiments so that the specimens will simultaneously undergo tension, compression and shear-type behavior.

Cuboidal metallic glass specimens having initial dimensions of 45 mm × 6mm × 4 mm measured along axis-1 (the length direction), axis-2 (the loading direction) and axis-3 (the transverse

direction), respectively, are used in this work to study the deformation characteristics under three-point bending conditions. The three-point bending fixture used in this study has two adjustable cylindrical bottom rollers of diameter 5 mm and a cylindrical top roller of diameter 4 mm. All three rollers are made out of tool steel. For all the three-point bending experiments, we have used a constant span of distance 35mm between the centers of the bottom rollers which are fixed throughout the duration of the experiments. The three rollers acting as the three loading points are carefully aligned parallel to one another by making use of a specially designed jig. The same experimental procedure described above is followed, i.e. the BMG specimen is heated to the required final temperature using a heating rate of 20 °K/min and annealed at this final temperature for 10 min prior to loading. High temperature lubricant is also applied at the contact surfaces between the rollers and the metallic glass specimens to minimize frictional effects. We have conducted three-point bending experiments at three different ambient temperatures within the supercooled liquid region, i.e. 417 K, 422 K and 427 K. To achieve isothermal testing conditions, all three-point bending experiments were conducted with the

top roller moving into the metallic glass specimens at a low speed of 0.05 mm/s along the loading direction, i.e. axis-2.

To numerically simulate the three-point bending experiments, we use the initially-undeformed finite-element mesh shown in Fig. 5a meshed using the actual dimensions of the experimental three-point bending set-up and specimen sizes described above. Due to symmetry only 1/4th of the metallic glass specimen is analyzed, and it is meshed using 6900 Abaqus C3D8R continuum-brick elements. The top and bottom rollers are assumed to be rigid and are meshed using analytical rigid surfaces. Appropriate three-point bending boundary conditions are imposed on the metallic glass specimen. The top roller is moved into the metallic glass specimen at a speed of 0.05 mm/s along axis-2, i.e. the loading direction whereas the bottom roller is rigidly fixed from motion. As mentioned previously, axis-1 and axis-3 represents the length direction and the transverse direction of the metallic glass specimen, respectively. Furthermore, we have assumed frictionless contact between the metallic glass specimen and the rigid rollers. The metallic glass specimen is also taken to be fully-annealed at test temperatures of 417 K, 422 K and 427 K prior to deformation. Finally, all the three
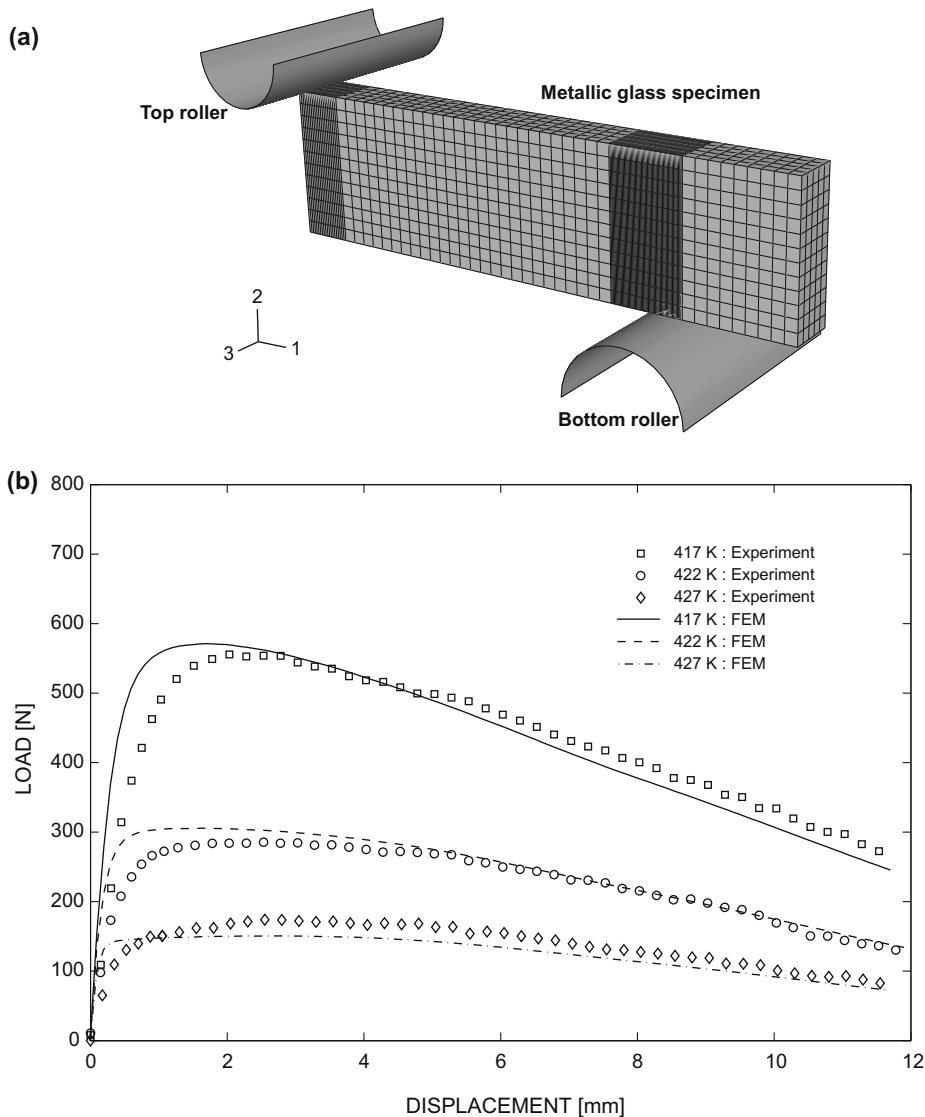

Fig. 5. (a) The initially-undeformed finite-element mesh for the 3-point bending simulations. Due to symmetry, only 1/4-th of the metallic glass specimen is modeled. The metallic glass specimen is meshed using 6900 Abaqus C3D8R continuum-brick elements whereas the top and bottom rollers are meshed using analytical rigid surfaces. (b) The experimentally obtained load-displacement data for the three-point bending experiments on the metallic glass specimen conducted at ambient temperatures of 417 K, 422 K and 427 K. Also shown are the numerically-simulated load-displacement curves. The top roller speed used in the experiments and simulations is 0.05 mm/s.
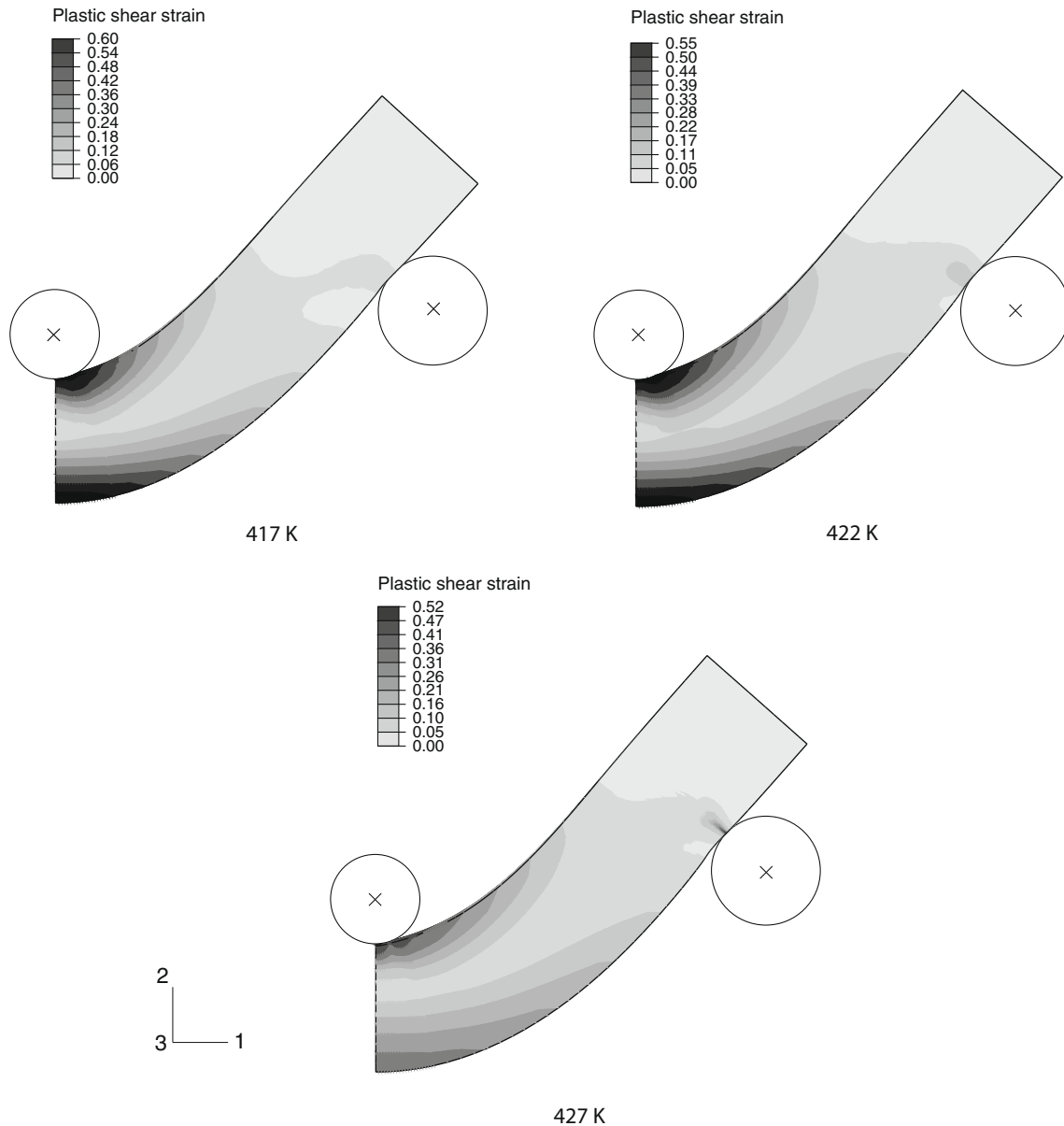
Fig. 6. The contours plastic shear strain in the deformed metallic glass specimen determined at the conclusion of the three-point bending finite-element simulations. These contour plots were obtained from the simulations conducted at ambient temperatures 417 K, 422 K and 427 K.

three-point bending simulations were conducted under *isothermal* conditions.

The top roller force versus its displacement curves determined from the three-point bending experiments described above are plotted in Fig. 5b along with the force vs. displacement curves obtained from the corresponding finite-element simulations conducted using the material parameters listed in Table 1. The experimental force–displacement curves are accurately predicted by the constitutive model. In particular, the experimental force–displacement curves show that once a peak load is reached, continued deformation will cause a softening in the force–displacement responses. This trend is well-reproduced by the constitutive model. As expected the experimentally-applied force required to sustain plastic deformation under three-point bending loading conditions *increases* with *decreasing* ambient test temperature, and this trend is also accurately predicted by the finite-element simulations.

The contours of the plastic shear strain in the deformed metallic glass specimen obtained at the conclusion of the

three-point bending simulations conducted above are shown in Fig. 6. These contour plots show that certain the sections of the metallic glass specimens have experienced relatively large plastic deformation.

To further investigate the nature of the multi-axial deformation during the three-point bend tests, we plot the deformed cross-section of the metallic glass specimens located directly under the top roller obtained at the conclusion of the three-point bending experiments in Fig. 7a. Also shown in Fig. 7a is the cross-section of the initially-undeformed physical specimen. For comparison, we show the predicted cross-section of the deformed metallic glass specimen located directly under the top roller obtained at the conclusion of the three-point bending finite-element simulations in Fig. 7b. From the plots shown in Fig. 7, we can also conclude that the constitutive model is able to predict the deformed geometry of the three-point bend specimens to good accord. The experimental results shown in Fig. 7a show a gradual tapering of the deformed specimen cross-section along axis-2 with the top line segment being the widest and the bottom line segment being the narrowest. As plotted in Fig. 7b, this
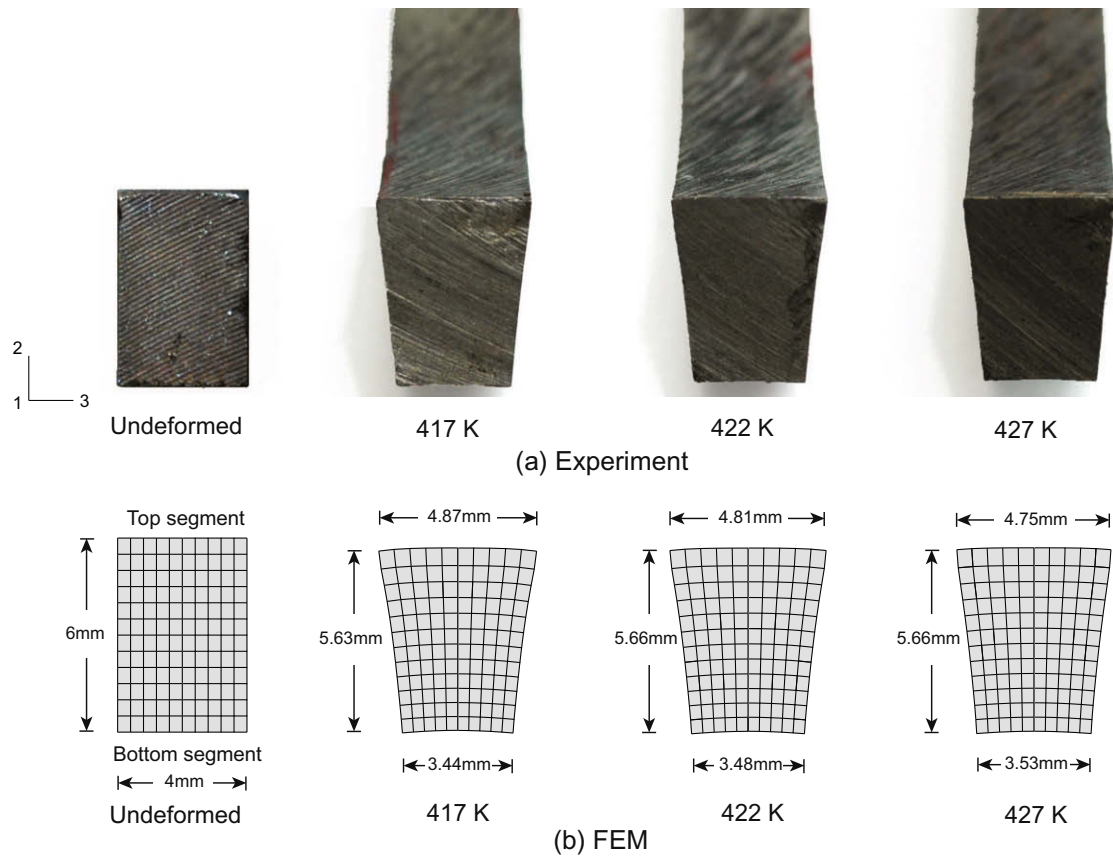
Fig. 7. The deformed cross-section of the metallic glass specimens located directly under the top roller determined at the conclusion of the three-point bending (a) experiments, and (b) finite-element simulations obtained at ambient test temperatures of 417 K, 422 K and 427 K. The experimentally-determined bottom vs. top line segments' deformed lengths for the three-point bending experiment conducted at an ambient temperature of 417 K, 422 K and 427 K are 3.48 mm by 4.87 mm, 3.43mm by 4.79 mm, and 3.47 mm by 4.73 mm, respectively. Also shown are the numerically-simulated bottom and top line segments' deformed lengths.

observed tapering of the deformed cross-section is also well-reproduced by the constitutive model.

3.2. Superplastic forming of a metallic glass component

At temperatures significantly below the glass transition temperature (θ_g), bulk metallic glasses exhibit insignificant macroscopic plastic strain and typically fractures by forming shear bands. Compared to its characteristics at temperatures below θ_g, metallic glasses exhibit very high formability at temperatures within the supercooled liquid region as its viscosity is much lower and hence the material is able to flow much more easily exhibiting superplastic-like deformation characteristics. In this Section, we will perform the superplastic forming process of a miniature gear component made from the La-based metallic glass specimen studied in the present work.

The geometry of the die used to form the miniature gear component is taken from the work Wang et al. (2005), and is shown in Fig. 8a. Wear resistant structural-steel material has been used for fabricating the required die. The gear-shaped die features are wire cut using electric discharge machining (EDM) on a 1.5 mm thick plate having dimensions of 15 mm × 15mm. An additional step of circular cross-section, having 4 mm diameter and 0.5 mm depth co-axial with the gear-shaped mold is end milled on top of the die, and this step shall be used to secure and align the metallic glass specimen axis along with the die axis during the forming experiment.

Cylindrical metallic glass specimens having a diameter 4 mm and height of 5 mm are machined out from the as-cast 5 mm thick

$La_{61.4}Al_{15.9}Ni_{11.35}Cu_{11.35}$ plates to be used as the initial specimens for superplastic forming. The end faces of the cylindrical metallic glass specimen are initially polished using 1200 grit silicon carbide paper and a thin film of molybdenum disulphide is coated on these surfaces to attain frictionless conditions during the metal forming process. The die surfaces which will come in contact with the deforming specimen are also coated with molybdenum disulphide to minimize frictional effects. The specimen is then placed concentrically with the die and allowed it to sit flat beneath the step on top of the die. This assembly is later placed on top of the compression platen within the temperature chamber of the mechanical testing machine. The mechanical testing machine's compression platen would act as the forming punch forcing the material into the die. The specimen is heated to the required temperature using a typical ramping rate of 20 °C per minute and held at the desired test temperature for 10 min prior to loading. By this time, the temperature of the die and the metallic glass specimen would be equal to the ambient testing temperature.

Using the geometry for the die and metallic glass specimen as described above, we conduct finite-element simulations of the superplastic forming process using the initially-undeformed mesh as shown in Fig. 8b. Due to symmetry, only 1/12-th of the whole die and metallic glass specimen assembly is modeled. The die is assumed to be rigid and it is meshed using 1398 Abaqus R3D4 rigid elements. The metallic glass specimen is meshed using 98704 Abaqus C3D8R elements. The finite-element simulations were conducted using the material parameters listed in Table 1.

The superplastic forming experiments and simulations were performed with the die moving into the metallic glass specimen at a low
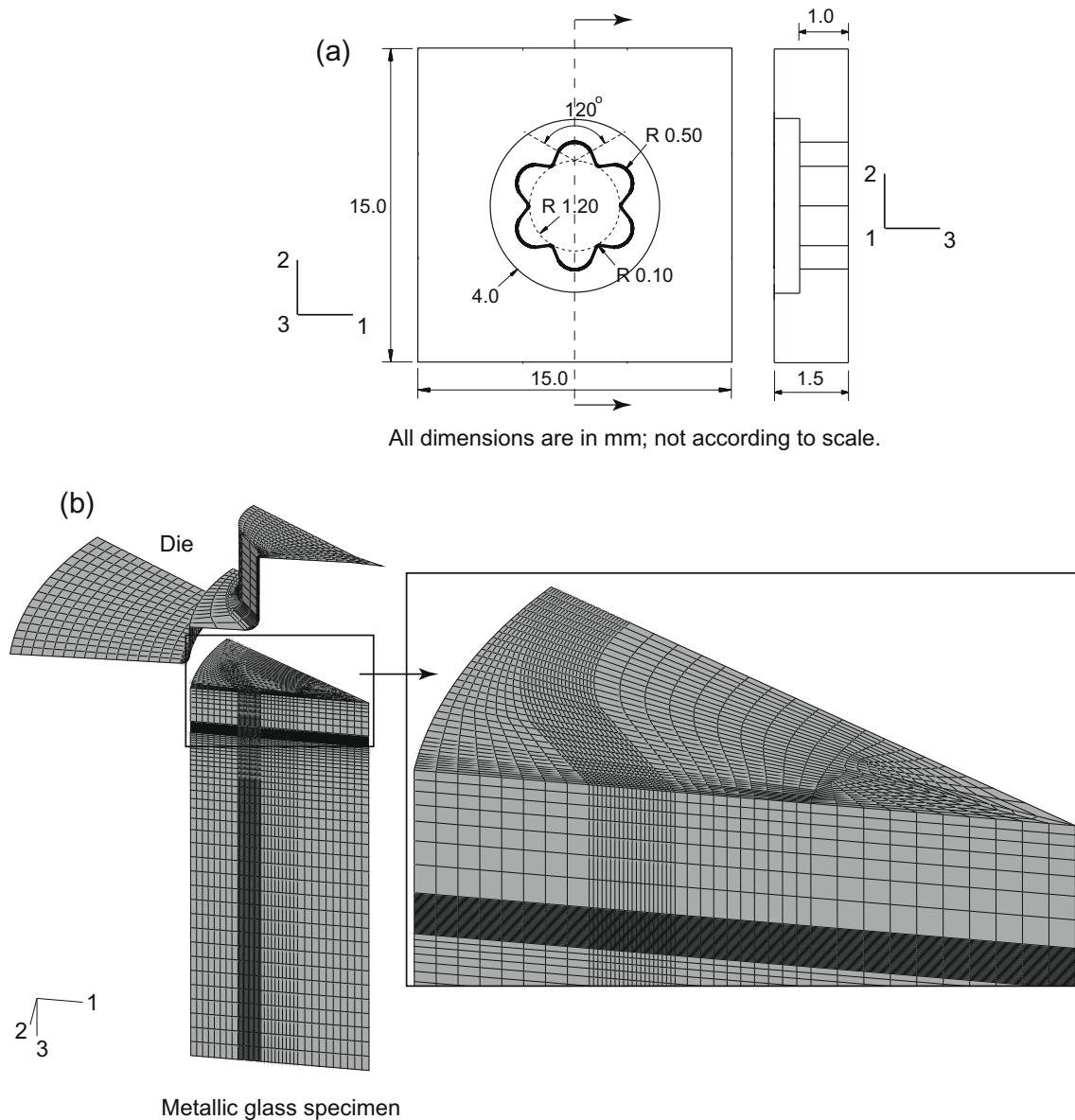
Fig. 8. (a) The geometry of the die used to form the miniature gear-shaped component. (b) The initial finite-element mesh showing 1/12-th of the actual set-up used for simulating the gear forming experiment. The mesh consists of 1398 Abaqus R3D4 rigid elements for the die and 98704 Abaqus C3D8R continuum elements for the metallic glass specimen.

loading rate of 1×10^{-2} mm/s. Therefore, the finite-element simulations were conducted assuming *isothermal* conditions. The experiments and simulations were conducted at two different ambient temperatures: 427 K and 432 K. The corresponding die applied load versus its displacement curves obtained from the superplastic forming experiments and simulations are plotted in Fig. 9. The experimental load-displacement curves are well-predicted by the present constitutive model. As shown by the experimental results in Fig. 9 the forming load *decreases* with *increasing* temperature. This trend is also accurately predicted by the constitutive model.

Starting from the origin, the experimental and simulated forming load-displacement curves shown in Fig. 9 can be divided into three segments: (1) a initial linear region where the metallic glass deforms elastically; (2) a plateau region where the load increases gradually with the metallic glass specimen flowing into the die cavity and consequently taking the shape of the die; and finally (3) a rapid increase in load where the metallic glass has already filled the die cavity completely with further deformation causing the flattening of the

remaining metallic glass material not occupying the die cavity space. Also shown in Fig. 9 are the corresponding images of the actual and simulated metallic glass specimen keyed to points *a* to *e* on the force–displacement curves of the superplastic forming experiment and simulation conducted at an ambient temperature of 432 K, respectively. These images pictorially depict the entire metal forming process through various stages, i.e. from the initial cylindrical specimen to the formation of the final miniature gear component. A qualitative comparison of the experimental results to the simulated results shows the ability of the constitutive model in accurately predicting the evolution of the miniature gear component geometry during the superplastic forming process.

4. Conclusion

The deformation behavior of the $La_{61.4}Al_{15.9}Ni_{11.35}Cu_{11.35}$ bulk metallic glass under uniaxial and multi-axial stress-states have been modeled using the constitutive equations of Thamburaja
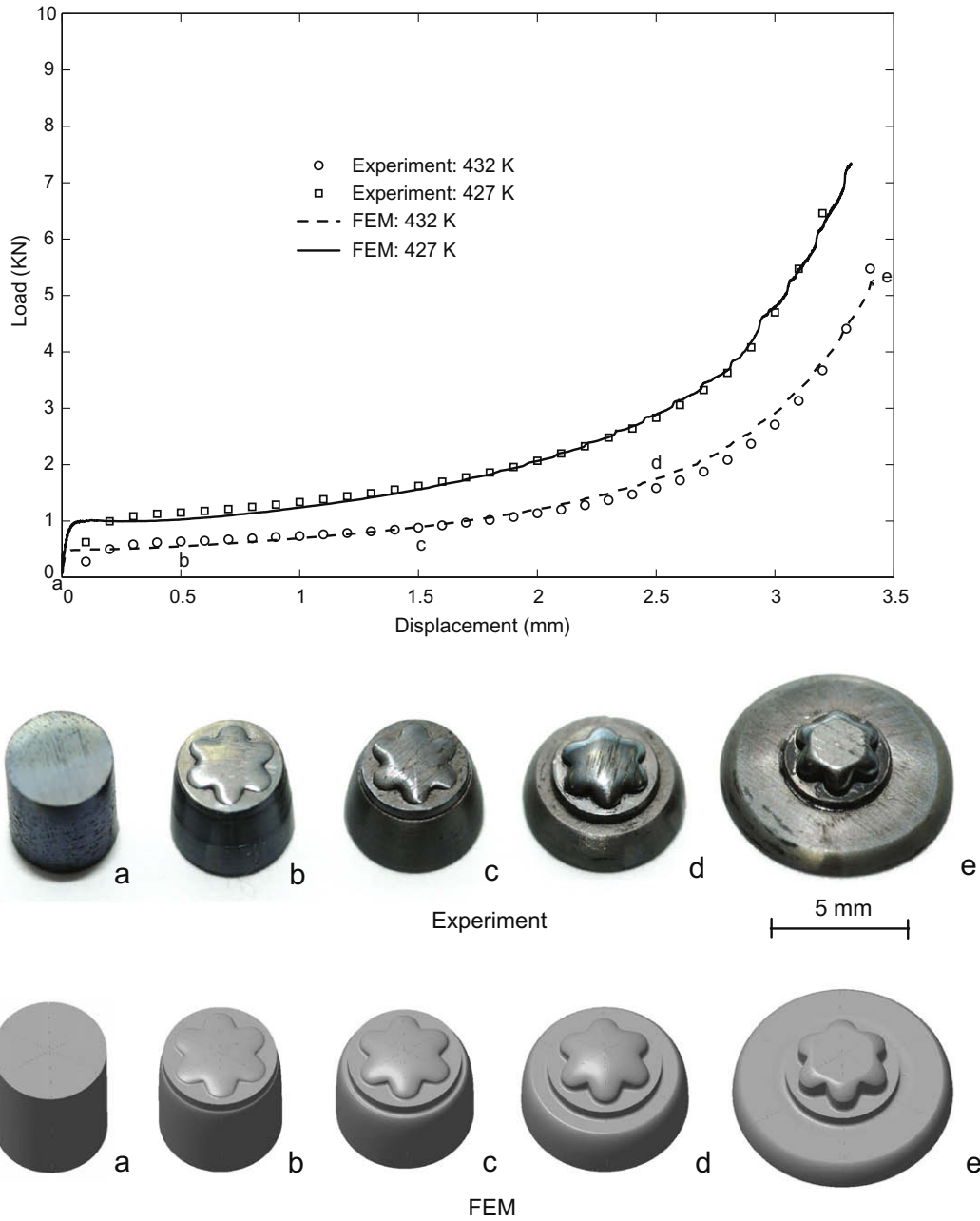
Fig. 9. The experimentally obtained force vs. displacement curves during forming of the gear-shaped metallic glass component at ambient temperatures of 427 K and 432 K. The corresponding predictions from the constitutive model are also plotted. The die speed used for the experiments and the simulations is 0.01 mm/s. Also shown are the experimental and simulated geometry of the metallic glass gear component keyed to points a to e on the force–displacement curves determined from the experiment and simulation conducted at an ambient temperature of 432 K, respectively.

and Ekambaram (2007) via its numerical-implementation into the Abaqus (2008) finite-element program. The material parameters in the constitutive model were fitted to match the stress vs. strain responses from a series simple compression experiments conducted under various strain rates at temperatures within the supercooled liquid region. With the constitutive parameters calibrated, force vs. displacement responses obtained from three-point bending and superplastic forming experiments performed at different temperatures within the supercooled liquid region were accurately predicted by the constitutive model. In particular, the constitutive model and finite-element simulations are also able to accurately reproduce the evolution of the specimen geometry during the deformation process under multi-axial stress-states.

Acknowledgements

References

Abaqus Reference Manuals., 2008. SIMULIA, Providence, R.I.
Argon, A., 1979. Plastic deformation in metallic glasses. Acta Metallurgica et Materialia 27, 47–58.
Chen, H., Kato, H., Inoue, A., 2000. A fictive stress model calculation of stress-overshoot: a nonlinear viscoelastic behavior in metallic glass. Japanese Journal of Applied Physics 39, 1808–1811.

Davis, L., Kavesh, S., 1975. Deformation and fracture of an amorphous metallic alloy at high pressure. Journal of Materials Science 10, 453–459.

De Hey, P., Sietsma, J., Van Den Beukel, A., 1997. Creation of free volume in amorphous pd-ni-p during high temperature deformation. Materials Science and Engineering A 226, 336–340.

Demetriou, M., Johnson, W., 2004. Modeling the transient flow of undercooled glass-forming liquids. Journal of Applied Physics 95, 2857–2865.

Donovan, P., 1989. A yield criterion for pd-ni-p metallic glass. Acta Metallurgica 44, 445–456.

Ekambaram, R., Thamburaja, P., Nikabdullah, N., 2008. On the evolution of free volume during the deformation of metallic glasses at high homologous temperatures. Mechanics of Materials 40, 487–506.

Ekambaram, R., Thamburaja, P., Nikabdullah, N., 2009. Shear localization and damage in metallic glasses at high homologous temperatures. International Journal of Structural Changes in Solids 1, 91–106.

Fried, E., Gurtin, M., 1994. Dynamic solid-solid transitions with phase characterized by an order parameter. Physica D 72, 287–308.

Heggen, M., Spaepen, F., Feuerbacher, M., 2004. Plastic deformation of pd-ni-cu bulk metallic glass. Materials Science and Engineering A, 1186–1190.

Henann, D., Anand, L., 2009. Fracture of metallic glasses at notches: effects of notch-root radius and the ratio of the elastic shear modulus to the bulk modulus on toughness. Acta Materialia 57, 6057–6074.

Huang, R., Suo, Z., Prevost, J., Nix, W., 2002. Inhomogeneous deformation in metallic glasses. Journal of the Mechanics and Physics of Solids 50, 1011–1027.

Jiang, Q., Zhang, G., Yang, L., Wang, X., Saksl, K., Franz, H., Wunderlich, R., Fecht, H., Jiang, J., 2007. La-based metallic glasses with critical diameter up to 30 mm. Acta Materialia 55, 4409–4418.

Kato, H., Chen, H., Inoue, A., 2008. Relationship between thermal expansion coefficient and glass transition temperature in metallic glasses. Scripta Materialia 58, 1106–1109.

Kato, H., Kawamura, Y., Inoue, A., Chen, H., 2001. Modeling of stress–strain curves for pd-ni-cu-p glass under constant strain-rate deformation. Materials Science and Engineering A 304, 758–762.

Kawamura, Y., Inoue, A., 1999. Superplastic forming of $zr_{65}Al_{10}Ni_{10}Cu_{15}$ metallic glass. Materials Science Forum, 373–378.

Kawamura, Y., Nakamura, T., Inoue, A., Masumoto, T., 1999. High-strain-rate superplasticity due to newtonian viscous flow in $La_{55}Al_{25}Ni_{20}$ metallic glass. Materials Transactions JIM 22, 794–803.

Kim, H., Kato, H., Inoue, A., Chen, H., Hong, S., 2004. Microforming of bulk metallic glasses: constitutive modelling and applications. Materials Transactions JIM 45, 1228–1232.

Lewandowski, J., Lowhaphandu, P., 1998. Effects of hydrostatic pressure on mechanical behaviour and deformation processing of materials. International Materials Reviews 43, 145–187.

Lewandowski, J., Lowhaphandu, P., 2002. Effects of hydrostatic pressure on the flow and fracture of a bulk amorphous metal. Philosophical Magazine A 82, 3427–3441.

Lewandowski, J., Shazly, M., Shamimi Nouri, A., 2006. Intrinsic and extrinsic toughening of metallic glasses. Scripta Materialia 54, 337–341.

Lowhaphandu, P., Montgomery, S., Lewandowski, J., 1999. Effects of superimposed hydrostatic pressure on flow and fracture of a Zr–Ti–Ni–Cu–Be bulk amorphous alloy. Scripta Materialia 41, 19–24.

Lu, J., Ravichandran, G., Johnson, W., 2003. Deformation behavior of the Zr–Ti–Cu–Ni–Be bulk metallic glass over a wide range of strain-rates and temperatures. Acta Materialia 51, 3429–3443.

Masuhr, A., Waniuk, T., Busch, R. Johnson, W., 1999. Time scales for viscous flow, atomic transport, and crystallization in the liquid and supercooled liquid states of Zr–Ti–Cu–Ni–Be. Physical Review Letters 82, 2290–2293.

Patnaik, M., Narasimhan, N., Ramamurty, U., 2004. Spherical indentation response of metallic glasses. Acta Materialia 52, 3335–3345.

Roth, S., Stoica, M., Degmova, J., Gaitzsch, U., Eckert, J., Schultz, L., 2005. Fe-based bulk amorphous soft magnetic materials. Journal of Magnetism and Magnetic Materials 304, 192–196.

Saotome, Y., Hatori, T., Zhang, T., Inoue, A., 2001. Superplastic micro/nano-formability of $La_{60}Al_{20}Ni_{10}Co_5Cu_5$ amorphous alloy in supercooled liquid state. Materials Science and Engineering A, 716–720.

Schroers, J., 2008. On the formability of bulk metallic glass in its supercooled liquid state. Acta Materialia 56, 471–478.

Spaepen, F., 1977. A microscopic mechanism for steady state inhomogeneous flow in metallic glasses. Acta Metallurgica et Materialia 25, 407–415.

Tan, H., Zhang, Y., Ma, D., Feng, Y., Li, Y., 2003. Optimum glass formation at off-eutectic composition and its relation to skewed eutectic coupled zone in the la based laal(Cu, Ni) pseudo ternary system. Acta Materialia 51, 4551–4561.

Thamburaja, P., Ekambaram, R., 2007. Coupled thermo-mechanical modelling of bulk-metallic glasses: theory, finite-element simulations and experimental verification. Journal of the Mechanics and Physics of Solids 55, 1236–1273.

Vormelker, A., Vatamanu, O., Kecskes, L., Lewandowski, J., 2008. Effects of test temperature and loading conditions on the tensile properties of a Zr-based bulk metallic glass. Metallurgical and Materials Transactions A 39, 1922–1934.

Wang, G., Shen, J., Sun, J., Huang, Y., Zou, J., Lu, Z., Stachurski, Z., Zhou, B., 2005. Superplasticity and superplastic forming ability of a Zr–Ti–Ni–Cu–Be bulk metallic glass in the supercooled liquid region. Journal of Non-Crystalline Solids 351, 209–217.

Wang, W., Dong, C., Shek, C., 2004. Bulk metallic glasses. Materials Science and Engineering R-Reports 44, 45–89.

Wesseling, P., Ko, B., Vatamanu, L., Shiflet, G., Lewandowski, J., 2008. Effects of annealing and pressure on devitrification and mechanical properties of amorphous Al-Ni-Gd. Metallurgical and Materials Transactions A 39, 1935–1941.

Zhang, X., Yong, Z., Hao, T., Yong, L., Chen, X., Chen, G., 2007. Micro-electro-discharge machining of bulk metallic glasses. Proceedings of HDP 2007, 213–216.